AIChE

Modeling the Thermochemical Degradation of Biomass Inside a Fast Pyrolysis Fluidized Bed Reactor

J. Bruchmüller
Energy Technology Research Group, Faculty of Engineering and the Environment, University of Southampton, Southampton SO17 1BJ, U.K.

B. G. M. van Wachem
Dept. of Mechanical Engineering, Imperial College London, London SW7 2AZ, U.K.

S. Gu
Energy Technology Research Group, Faculty of Engineering and the Environment, University of Southampton, Southampton SO17 1BJ, U.K.

Dept. of Civil Engineering, Xi'an Jiaotong-Liverpool University, Suzhou 215123, China

K. H. Luo
Energy Technology Research Group, Faculty of Engineering and the Environment, University of Southampton, Southampton SO17 1BJ, U.K.

Center for Combustion Energy, Dept. of Thermal Engineering, Tsinghua University, Beijing 100084, China

R. C. Brown
Center for Sustainable Environmental Technologies, Iowa State University, Ames, IA 50011

DOI 10.1002/aic.13705
Published online December 14, 2011 in Wiley Online Library (wileyonlinelibrary.com).

A fast pyrolysis process in a bubbling fluidized bed has been modeled, thoroughly reproduced and scrutinized with the help of a combined Eulerian/Lagrangian simulation method. The 3-D model is compared to experimental results from a 100 g/h bubbling fluidized bed pyrolyzer including such variables as particle composition at the outlet and gas/vapor/water yields as a function of fluidization conditions, biomass moisture concentrations, and bed temperatures. Multiprocessor simulations on a high-end computer have been carried out to enable the tracking of each of the 0.8 million individual discrete sand and biomass particles, making it possible to look at accurate and detailed multiscale information (i.e., any desired particle property, trajectory, particle interaction) over the entire particle life time. The overall thermochemical degradation process of biomass is influenced by local flow and particle properties and, therefore, accurate and detailed modeling reveals unprecedented insight into such complex processes. It has been found, that the superficial fluidization velocity is important while the particle moisture content is less significant for the final bio-oil yield. © 2011 American Institute of Chemical Engineers *AIChE J,* 58: 3030–3042, 2012

Keywords: fast pyrolysis, drying, discrete element method, biomass, fluidized bed, distributor plate, particle entrainment

Introduction

Fast pyrolysis is the most widely used process to convert biomass into high fractions of liquid bio-oil.[1] In fast pyrolysis, organic material (often wood/biomass) is heated rapidly to temperatures between 700 and 850 K in the absence of oxygen to produce liquids, char, and gas. The final liquid bio-oil yield depends on the amount of condensible gases (tar) created by primary pyrolysis reactions and the amount of tar which is reduced by thermal cracking, repolymerization and recondensation, which are referred to as secondary pyrolysis reactions. The remaining solid, in case biomass is sufficiently depleted into char/ash, and noncondensible gases (CO_2, CO, H_2, CH_4, etc.) are both entrained with the fluidizing gas. Bubbling fluidized beds are often favored over other reactor technologies for liquid bio-oil production due to high achievable oil-yields, low complexity and ease in scale-up.

Modeling fast pyrolysis in bubbling fluidized beds is an attractive opportunity to get information which is very difficult to obtain experimentally as tar inside hot fluidized beds causes trouble for most measuring devices and would darken windows for visual observations. Simulations have benefits in providing small-scale, local and detailed information such as particle temperatures, porosities, gas or particle velocities to improve the understanding of local phenomena prevailing complex processes such as fast pyrolysis. Different numerical

Correspondence concerning this article should be addressed to S. Gu at s.gu@soton.ac.uk.

simulation strategies to model gas–solid fluidized beds have been reviewed by van der Hoef et al.[2] In most cases, multiphase modeling of the hydrodynamic behavior in fluidized beds is either achieved by an Euler-Euler (two-fluid) or Euler-Lagrange approach. Inconsistencies and erroneous predictions occur when two-fluid models are applied to dilute fluid-particle flows.[3] Desjardin et al.[4] pointed out that two-fluid models are unable to correctly capture particle trajectory crossing and particle segregation is artificially over predicted for finite Knudsen numbers. Furthermore, no information can be obtained from two-fluid models about the residence time of individual reacting particles, representing highly valuable key-information for assessing the overall process. Although computationally expensive, the Eulerian-Lagrangian approach (or the CFD-DEM approach) has the highest potential to realistically reveal thermochemical processes in granular multiphase flow applications. DEM models are able to accurately predict interparticle and interphase exchange of mass, momentum and energy at the individual particle level. Therefore, trajectories, temperature, composition (reaction rates) and any other additional particle information are more reliably and more naturally included than in Eulerian formulations which are based on spatial averaging techniques with strong simplifications made on the particle kinematics and thermodynamics. The accuracy on the particle level is essential to study effects like thermochemical degradation, shrinkage, breakage, segregation, mixing and entrainment.

The discrete element method was first proposed by Cundall[5] and has found application in various chemical engineering problems in rather small fluidized beds.[6] Due to its complexity, DEM simulations are mostly performed in 2-D or quasi 3-D (domain width is one or slightly more particle diameters). Erroneous predictions in 2-D/quasi 3-D simulations have been found based on porosity,[7] the particle contact number, segregation, drag and interparticle percolation[8] so that other simulation strategies such as parallel computing techniques, periodic-boundaries or novel numerical time integration schemes[9] are favored to maintain the computational feasibility.

Particle heat-transfer,[10] coal/char combustion[11,12] and wood gasification[13] have been modeled with CFD/DEM, although the particle size in these studies are far bigger than the actual sand used in ordinary experimental beds. Rabinovich et al.[14] used a CFD-DEM model to study fast pyrolysis although the bed conditions used are strongly simplified (e.g., 500 sand particles). Papadikis et al.[15–17] carried out a series on fast pyrolysis simulations where the gas and sand phase are modeled by a two-fluid approach (Eulerian approach) and biomass is considered by means of very few (1–3) Lagrangian particles. Herein, any discrete biomass information is rather arbitrary than statistically averaged over many continuously tracked biomass particles, particle–particle interactions are strongly simplified by considering artificially generated drag and the biomass movement (trajectory) is limited to two dimensions.

Present research needs in the field of fast pyrolysis modeling have been summarized by Di Blasi.[18] These needs are, amongst others, related to (1) more detailed inclusion of extra-particle processes, (2) the accurate prediction of conversion times and global decomposition rates, and (3) incorporation of structural changes of biomass, dependence on physical properties on conversion conditions and detailed mechanisms of pyrolysis reactions. Furthermore, the ejection mechanisms and the origin of ejected particles from the bed into the freeboard can be crucial and have only been postulated while further studies are needed to elucidate particle entrainment.[19] DEM is able to account for all these shortcomings of previous research efforts.

This work investigates fast pyrolysis from a particle-scale perspective without disregarding the largest scales present in fluidized beds. Mixing, segregation and entrainment of the biomass phase in the reactor are analysed and the impact on and change of particle properties throughout their entire particle life-time has been monitored. The modeled process is semicontinuous in the sense that it is modeled from the moment where biomass feeding is started to the moment where the main variables (i.e., the amount of gas/tar/water in the gas phase) are converged to steady-state, which has been approximately achieved after 5 s.

Table 1. Gas-Phase Conservation Equations and Interphase Exchange Equations Used

$$\frac{\partial(\varepsilon\rho_{\mathrm{f}})}{\partial t}+\nabla\cdot(\varepsilon\rho_{\mathrm{f}}\vec{u}_{\mathrm{f}})=S$$

$$\frac{\partial(\varepsilon\rho_{\mathrm{f}}\vec{u}_{\mathrm{f}})}{\partial t}+\nabla\cdot(\varepsilon\rho_{\mathrm{f}}\vec{u}_{\mathrm{f}}\vec{u}_{\mathrm{f}})=-\varepsilon\nabla P+\nabla\cdot(\varepsilon\bar{\bar{\tau}})+\rho_{\mathrm{f}}\varepsilon\vec{g}-\sum_{i=1}^{n}\frac{V_{\mathrm{p},i}\beta}{(1-\varepsilon)}(\vec{u}_{\mathrm{f}}-\widetilde{\vec{u}_{\mathrm{p},i}})\delta(x-x_{\mathrm{p},i})+S\vec{u}_{\mathrm{f}}$$

$$\frac{\partial(\varepsilon\rho_{\mathrm{f}}c_{\mathrm{p,f}}T_{\mathrm{f}})}{\partial t}+\nabla\cdot(\varepsilon\rho_{\mathrm{f}}\vec{u}_{\mathrm{f}}c_{\mathrm{p,f}}T_{\mathrm{f}})=\nabla\cdot(\varepsilon\lambda_{\mathrm{f}}\nabla T_{\mathrm{f}})+Q_{\mathrm{f}}$$

$$\frac{\partial(\varepsilon\rho_{\mathrm{f}}Y_{\mathrm{i}})}{\partial t}+\nabla\cdot(\varepsilon\rho_{\mathrm{f}}\vec{u}_{\mathrm{f}}Y_{\mathrm{i}})=\nabla\cdot(\varepsilon\rho_{\mathrm{f}}\Gamma_{\mathrm{f}}\nabla Y_{\mathrm{i}})+S_{\mathrm{i}}$$

$$\beta=\frac{3}{4}C_{\mathrm{D}}|\widetilde{\vec{v}_{\mathrm{f}}}-\vec{v}_{\mathrm{p}}|\frac{\rho_{\mathrm{f}}(1-\varepsilon)(\varepsilon)^{-1.65}}{d_{\mathrm{p}}}$$

$$C_{\mathrm{D}}=\begin{cases}\frac{24}{\varepsilon Re_{\mathrm{p}}}(1+0.15(\varepsilon Re_{\mathrm{p}})^{0.687}) & \text{if } \varepsilon Re_{\mathrm{p}}<1000\\ 0.44 & \text{if } \varepsilon Re_{\mathrm{p}}\geq 1000\end{cases}$$

Symbols are explained in the Nomenclature.

Theoretical Model

Fluid-phase modeling

The fluid-phase is modeled as a continuum, known as an Eulerian type model and is considered to be a mixture of nitrogen as the inert fluidization gas and water vapor, tar and noncondensible gases released during the degradation process of biomass particles. The volume-averaged fluid phase continuity, momentum, energy and species transport equations are solved for each time step associated with the fluid. The differential equations describing the fluid phase are given in Table 1. Tildes are used to indicate interpolated properties between the fluid and particle grid—particle properties on the particle grid are interpolated to the fluid mesh (as seen by the fluid) or vice-versa. The interphase momentum exchange coefficient β is modeled via the well-known Wen and Yu drag correlation[20] which is valid over a broad range of conditions. The term $\delta(x - x_{\mathrm{p},i})$ represents the Dirac delta function, ensuring the momentum transfer is considered only at the particle locations.[7] The shear stress tensor $\bar{\bar{\tau}}$ is assumed to be Newtonian. Turbulence is suppressed in dense particle regions due to high solid volume fractions even for moderately high Reynolds numbers (<2000)[2] while in dilute particle regions (bubbles) turbulence might affect only slightly particle trajectories or reactions. To assume laminar flow is therefore believed to be a good approximation.[21,22] The particle motion in the freeboard is assumed to be controlled by splashing rather than turbulent diffusion.[23]

In this work, no chemical reactions are considered in the gas phase so that there is no specific need to resolve turbulence.

Particle-phase modeling

The translational and rotational particle motion is modeled by the discrete element method at an individual particle level by using Newton's second law of motion according to Eqs. 1 and 2.

$$m_{\mathrm{p}}\frac{d\vec{u}_{\mathrm{p}}}{dt}=\vec{F}_{\mathrm{g}}-V_{\mathrm{p}}\nabla P+\frac{V_{\mathrm{p}}\beta}{(1-\varepsilon)}(\widetilde{\vec{u}_{\mathrm{f}}}-\vec{u}_{\mathrm{p}})+\sum_{\mathrm{col}}(\vec{F}) \tag{1}$$

$$I_{\mathrm{p}}\frac{d\vec{\omega}_{\mathrm{p}}}{dt}=\sum_{\mathrm{col}}(\vec{T}) \tag{2}$$

where $\vec{u}_{\mathrm{p}}$ and ω_{p} are the translational and rotational particle velocity vectors, $\vec{F}_{\mathrm{g}}$ includes gravity and buoyancy forces, P is the local normal pressure, $\widetilde{\vec{u}_{\mathrm{f}}}$ represents the undisturbed local fluid velocity, $I_{\mathrm{p}}=\frac{2}{5}m_{\mathrm{p}}r_{\mathrm{p}}^2$ is the moment of inertia and $\vec{T}$ is the torque acting on that particle. The interparticle collision forces $\vec{F}$ are solved by a soft-sphere approach based on the combination of a nonlinear Hertzian spring model combined with a dampening model for the normal direction[24] and a model representing the tangential forces during impact based on Mindlin and Deresiewicz.[25]

A detailed description of the implemented equations for the collision model can be found in our previous work.[26] The collision model is based on physical particle and wall properties with the following values: Young's modulus $E = 5 \times 10^5$ Pa, Poisson ratio $\sigma = 0.3$, friction coefficient $\mu = 0.3$ and the coefficient of restitution $e = 0.95$. All values are equally valid for walls and particles. Mikami et al.[27] argued that once particles collide sufficiently often they behave like a continuum and, accordingly, the computed DEM results are not sensitive to stiffness parameters. For other conditions, these parameters might represent a potential risk to obtain erroneous results from DEM simulations representing a drawback compared to two fluid models.

Heat transfer at the particle surface is considered to occur by a combination of convective and radiative mechanisms. Particle–particle radiation must be included in fast pyrolysis studies to accurately predict the tar yield.[28] The conductive interparticle heat transfer contribution compared to convection and radiation in fluidized beds is only of minor importance[10,11,28] and has not been considered in this study. Latent heat during water evaporation and heat of reaction during pyrolysis are applied. In that case, the zero-dimensional particle energy equation is expressed as:

$$\begin{aligned}m_{\mathrm{p}}c_{\mathrm{p}}\frac{\partial T_{\mathrm{p}}}{\partial t}&=-hA(T_{\mathrm{p}}-\widetilde{T_{\mathrm{f}}})-\omega\sigma A(T_{\mathrm{p}}^4-T_{\mathrm{bed}}^4)\\&-H_{\mathrm{evap}}\Delta S_{\mathrm{H_2O}}-H_{k_1/k_2/k_3}\Delta S_{1/2/3}\end{aligned} \tag{3}$$

where ω is the particle emissivity and the Stefan Boltzmann constant is $\sigma = 5.67 \times 10^{-8}$ W/(m^{2}K^4). $\widetilde{T_{\mathrm{f}}}$ represents the interpolated fluid temperature as seen by the particle, H is the heat of reaction to evaporate water (latent heat) or one of the three pyrolysis reactions discussed in the next section and ΔS is the source term of the reactant. Due to low gas emissivities, gas radiation is not considered. The bed temperature T_{bed} is averaged over all particle temperatures in the present and adjacent particle cells given as:

$$T_{\mathrm{bed}}=\frac{1}{N_{\mathrm{nb}}+1}\left(T_{\mathrm{p}}+\sum_{i=1}^{N_{\mathrm{nb}}}T_{\mathrm{p},i}\right). \tag{4}$$

The convective heat-transfer coefficient $h = Nu\lambda_{\mathrm{f}}/d_{\mathrm{p}}$ for individual particles in bubbling beds is taken from the *Nu* correlation of Gunn[29] valid for a wide range of particle volume fractions (0…0.65).

$$\begin{aligned}Nu=&(7-10\varepsilon+5\varepsilon^2)\,(1+0.7Re_{\mathrm{p}}^{0.2}Pr^{1/3})\\&+(1.33-2.4\varepsilon+1.2\varepsilon^2)\,Re_{\mathrm{p}}^{0.7}Pr^{1/3}\end{aligned} \tag{5}$$

Drying and pyrolysis model

All particles in this work are treated as thermally thin where any transport mechanism within the particle is negligible. To conserve each solid or liquid species *i*, the general conservation equation is solved according to:

$$\frac{\partial\Phi_i}{\partial t}=S_i. \tag{6}$$

In fast pyrolysis applications, biomass particles experience very high heating rates and drying occurs almost regardless of moisture concentration gradients between surface and the local gas environment. Therefore, drying can be seen and simplified as a boiling process around 373 K by a thermodynamic balance between the energy needed to evaporate water and the energy transferred from the local surrounding to the particle. In this model, evaporation takes place when $T > T_{\mathrm{evap}}$ while the amount of water exchanged between the particle and the local gas environment is given by its source term as:

$$S_{\mathrm{H_2O}}=MIN\left(\frac{(T-T_{\mathrm{evap}})m_{\mathrm{p}}c_{\mathrm{p}}}{H_{\mathrm{evap}}\Delta t},\ \frac{Ym_{\mathrm{p}}}{\Delta t}\right). \tag{7}$$

The first term is limited by the energy or heat supplied to the particle while the second term is limited by the amount of remaining water left in the particle. After updating the water content *Y*, particle density and heat capacity is modified according to Eqs. 8 and 9, respectively.

$$\rho_{\mathrm{p}}=\frac{1}{\frac{Y}{\rho_{\mathrm{H_2O}}}+\frac{(1-Y)}{\rho_{\mathrm{DS}}}} \tag{8}$$

$$c_{\mathrm{p}}=c_{\mathrm{p,H_2O}}Y+c_{\mathrm{p}},\mathrm{DS}(1-Y) \tag{9}$$

The thermochemical degradation process of biomass can be modeled in different ways.[18] In this work, primary pyrolysis is modeled by a competitive generalized reaction scheme proposed by Miller and Bellan.[30] The model is based on a superposition of kinetics of the primary components of biomass: cellulose, hemicellulose, and lignin as depicted in Figure 1. Multistep, first-order, irreversible Arrhenius reactions are used where all kinetic parameters are summarized in Table 2. This pyrolysis mechanism is widely used for cellulose[31] and has been extended in the same way by Miller and Bellan[30] for the other two components. The model is based on a re-examination of literature data and found to be capable of making robust predictions of pyrolysis behavior for a variety of conditions and feedstocks.[30]

The initialization reaction (k_1) is thought of as a repolymerization step and does not produce any mass change or

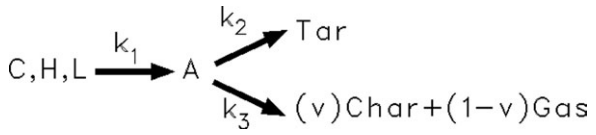

Figure 1. Semiglobal multicomponent mechanism for wood pyrolysis.

reaction heat. Therefore, wood is modeled as a composition of the three activated and nonactivated components as $X_{\mathrm{Wood}} = X_{\mathrm{C}} + X_{\mathrm{H}} + X_{\mathrm{L}} + X_{\mathrm{AC}} + X_{\mathrm{AH}} + X_{\mathrm{AL}}$. Furthermore, all mass fractions X are based on the initial dry solid wood mass, so that the equation $X_{\mathrm{Wood}} + X_{\mathrm{Char}} + X_{\mathrm{Gas}} + X_{\mathrm{Tar}} = 1$ is valid at any time during the simulation. Mass fractions for gas and tar are recorded for postprocessing reasons only. For each individual biomass particle an additional set of nine ordinary differential equations of the form given in Eq. 6 are solved for the pyrolysis model; for each activated and nonactivated component and the three products tar, char and gas. Due to the small biomass size, intraparticle secondary tar reactions are negligible[32] so that condensible and noncondensible gases are released at the particle surface instantaneously. A particle property Φ is updated linearly depending on its composition as:

$$\Phi = \Phi_{\mathrm{Char}} + (\Phi_{\mathrm{DS}} - \Phi_{\mathrm{Char}})X_{\mathrm{Wood}} \tag{10}$$

for $\Phi = \rho, c_{\mathrm{p}}$ as given in Table 3. Shrinkage during the drying process is neglected while during pyrolysis mass-proportional shrinkage[13,33,34] is assumed for each biomass particle. To conserve mass at any instant of time, the biomass particle diameter shrinks according to:

$$d_{\mathrm{p}} = \sqrt[3]{\frac{6}{\pi}\frac{m_{\mathrm{p}}}{\rho_{\mathrm{p}}}}. \tag{11}$$

It is further assumed that reactions are uniform throughout the particle and the ash layer (if exists) peels off instantaneously (see Figure 2). Although, shrinkage has a negligible effect on pyrolysis for small particles,[35] the remaining char particle volume and mass strongly affect particle trajectories on its way out of the reactor. High heating rates produce only little char formation[36] so that without particle shrinkage char entrainment would be highly over-predicted.

Solution procedure

The CFD code called MultiFlow (www.multiflow.org) has been used to model the work described herein and other previous CFD-DEM studies.[26,37,38] The particle phase is updated by solving the second law of Newton with a variable time-stepping routine by the well-known Verlet scheme[39] at each particle time step. The drying and pyrolysis model updates particle properties like temperature, density, diameter, heat capacity, and species composition at each fluid time step. Interparticle and particle-wall collisions are modeled by the soft-sphere discrete element method, where the solution method is well documented in the literature.[5,40] Coupling between the CFD and DEM model is achieved over the Wen and Yu[20] drag correlation, which is solved at every particle time-step. Recoupling of the drag force to the fluid phase takes place before the fluid phase calculations. The explicit update of the particle-phase has a much smaller time-scale ($\Delta t_{\mathrm{p}} \approx 2e^{-6}s$) compared to the implicitly solved fluid-phase ($\Delta t_{\mathrm{f}} = 5e^{-5}s$). A collocated finite volume method is used to predict the fluid flow field—using Rhie and Chow interpolation[41] for the stabilization of pressure and velocity coupling. Second-order backward Euler time discretization is used, while spatial discretization is achieved for nonconvective terms by the second-order central difference scheme and convective fluxes are approximated by a second-order upwind scheme. All partial differential equations are solved in a fully coupled manner, where the subset of linearized equations is solved by an additionally stabilized version of the Krylov Subspace Method (BiConjugate Gradient Squared).

The code is made parallel with MPI libraries and simulations were carried out on the UK national supercomputer HECToR Phase 2a (2.3 GHz, 192 cores in total distributed on 48 quad cores). Simulations required 80,000 CPU hours to obtain the first 5 s real time of pure sand fluidization. Biomass inside the reactor increased the computational expense so that 320,000 CPU hours were needed to accomplish the remaining 5 s real time. Low-temperature runs (T = 699 K) were slightly faster. Future work is planned to optimize the computational feasibility.

Experiments and simulation setup

Experiments have been performed at Iowa State University on a cylindrical fast pyrolysis bubbling fluidized bed reactor, with dimensions shown in Figure 4. An outside-cooled side pipe (attached radially 2.54 cm from the bottom) feeds fine red oak biomass particles with a screen size of 500 μm by a rotating shafted screw feeder with a rate of 100 g/h into the reactor. Nitrogen, water vapor, char particles, condensible and noncondensible gases leave the reactor through the outlet at the top where they get separated subsequently by traveling through cyclones, condensers and an electrostatic precipitator. Electrical heaters surrounding the reactor vessel are used to maintain pyrolysis at the desired reaction temperature and to ensure to a best degree adiabatic wall conditions. After preheating inside the plenum, pure nitrogen enters the bottom perforated distributor plate and fluidizes the sand bed. The distributor plate consists of 31 holes with a diameter of 1.65 mm each while the bottom distributor plate in the simulation has an inlet velocity of zero except for the 31 cell faces colored black in Figure 3b. The nitrogen flow through these 31 cells is thought to be a better approximation than the often assumed plug flow through all inlet

Table 2. Kinetic Parameters for the Three Main Components of the Generalised Biomass Model[30]

	Components			Reaction Heat/
	Cellulose (C)	Hemicellulose (H)	Lignin (L)	References
k_1	$2.80 \times 10^{19}\ \exp(-242.4/RT)$	$2.10 \times 10^{16}\ \exp(-186.7/RT)$	$9.60 \times 10^{8}\ \exp(-107.6/RT)$	0 kJ/kg
k_2	$3.28 \times 10^{14}\ \exp(-196.5/RT)$	$8.75 \times 10^{15}\ \exp(-202.4/RT)$	$1.50 \times 10^{9}\ \exp(-143.8/RT)$	+255 kJ/kg
k_3	$1.30 \times 10^{10}\ \exp(-150.5/RT)$	$2.60 \times 10^{11}\ \exp(-145.7/RT)$	$7.70 \times 10^{6}\ \exp(-111.4/RT)$	−20 kJ/kg
v	0.35	0.60	0.75	–
Red oak	46.9%	31.8%	21.3%	43

Table 3. Property Settings for the Particle and Fluid Phase

Property	Value	Unit	Sources
Wood specific heat (dry)	$c_{p,DS} = 1112.0 + 4.85\ T_p$	J/kgK	44
Char specific heat	$c_{p,Char} = 1003.2 + 2.09\ T_p$	J/kgK	45
Sand specific heat	$c_{p,Sand} = 860$	J/kgK	46
Red oak density (dry)	$\rho_{DS} = 660$	kg/m^3	35
Char density	$\rho_{char} = 350$	kg/m^3	47
Sand density	$\rho_{sand} = 2600$	kg/m^3	48
Solid emissivity	$\omega = 0.8$	–	10
Fluid density	$\rho_f = \frac{\widetilde{p}}{RT_f} \sum_i W_i Y_i$	kg/m^3	46
Sand diameter	$d = 0.52 \times 10^{-3}$	m	–
Initial biomass diameter	$d = 0.5 \times 10^{-3}$	m	–
Initial moisture content	$X = 0.161/0.07$	Kg_{H_2O}/kg_{DS}	–
Superficial gas velocity	$u_0 = 0.365/0.760 (u_0 = 1.3/3u_{mf})$	m/s	–
Number of sand particles	$N = 600{,}711$	–	–
Number of wood particles fed	$N = 37{,}724/36{,}764$	p/s	–

cells. All simulations in this article have been performed with a distributor plate except in section ''Fluidization of Sand'' where the fluidization behavior has been compared between a plug flow and multiorifice distributor plate inlet. The reactor has been recently modified after the process has been numerically investigated by Xue et al.[42] They have used a few different geometrical dimensions and initial/boundary conditions different to the ones used in this work.

The gas flow through the plenum and the particle feeding process in the attached feeding tube are not modeled. Biomass particles (black color) are inserted at the side of the domain as shown in Figure 4 and travel with the same constant feeding speed towards the bed centre. This resembles biomass feeding by a screw which presses the biomass into the reactor without using a carrier gas. Particle trajectories are updated normally according to the second law of Newton as soon as they made space for a new batch of virgin biomass particles to be inserted. As particles can only be inserted into voids (no artificial overlaps with other particles are allowed), a circular layer of nonmoving sand particles (gray color) along the wall is simulated to avoid that other particles enter that area. In the simulation, a batch consists of 318 biomass particles, which are inserted simultaneously. To achieve a feeding rate of 100 g/h, roughly 115 batch injections are made every second. This corresponds to roughly 37,000 virgin biomass particles entering the domain per second. This depends slightly on the chosen initial biomass moisture content of 7.0 or 16.1%. The composition of biomass in terms of cellulose, hemicellulose and lignin are typical for red oak (see Table 2). Extractives and ash content are incorporated in the hemicellulose component as proposed by Miller and Bellan.[30] In the model, biomass feeding is started after stable fluidization which is achieved in about 5 s of real time. Silica sand is used as the bed material with a mean particle diameter of 520 μm. Nitrogen, water vapor, condensible and noncondensible gases are modeled as individual species in the Euler gas phase. Nitrogen enters the bed from the bottom with a uniform temperature of 758/699 K and a mass flow rate of 52/42/26 L/min. The thermal conductivity, heat capacity and dynamic viscosity of the fluid have been assumed to be that of nitrogen at a pressure of 105 Pa and the selected pyrolysis temperature. Table 3 summarizes all property settings for the particle and fluid phase.

The initial sand and gas temperature in the domain are set equal to the inlet gas temperature of 758/699 K. It has been assumed that injected virgin biomass particles enter the domain with a temperature of 323 K. At walls, adiabatic and no-slip boundary conditions for the fluid-phase are applied while particles are allowed to slip freely. Energy transfer between particles and walls are neglected (zero-flux boundary condition). For the bottom distributor plate, Dirichlet boundary conditions are employed for all fluid variables, while particles experience the same boundary conditions as for walls. Particles are removed instantaneously when they reach the outlet at the top of the domain. The pressure at this boundary is fixed to a reference value of 1.013×10^5 Pa. The fluid velocity is calculated from that pressure and Neumann boundary conditions are applied for the temperature and species mass fractions requiring a fully developed fluid flow.

The following major assumptions and justifications are made for the simulation work and can be summarized as follows:

1. In this work, all biomass particles are treated as zero-dimensional thermally thin point sources although $Bi \approx 0.75$. According to Bryden and Hagge,[35] particles belong to the thermally thick regime if $0.2 < Bi < 10$, indicating temperature and species gradients inside particles but do not necessarily affect drying or pyrolysis times. Koufopanos et al.[32]

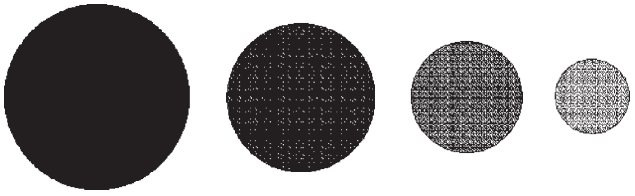

Figure 2. The applied progressive shrinkage mechanism for biomass particles.

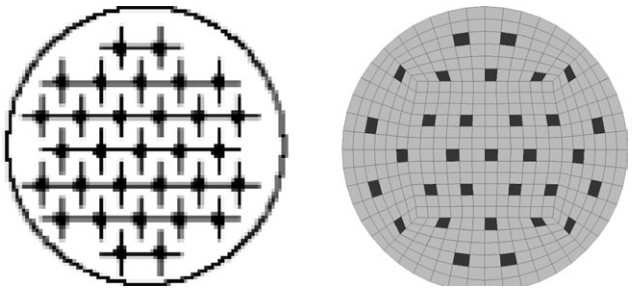

Figure 3. Perforated bottom distributor plate in (a) the experiment and (b) the simulation.

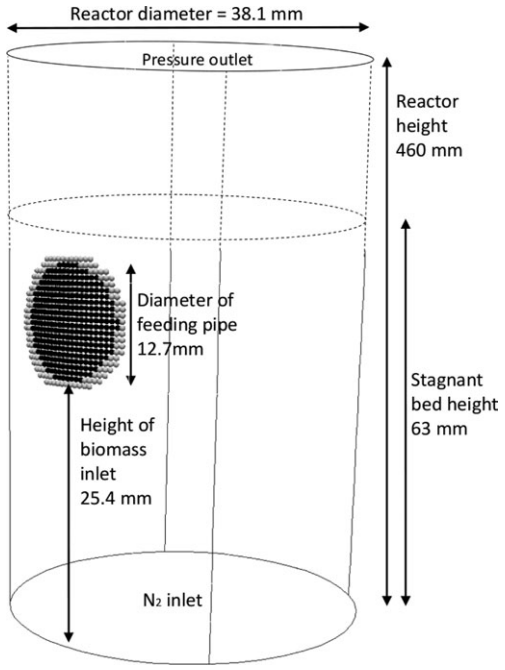

Figure 4. Reactor dimensions including one batch of biomass particles (black) surrounded by non-moving sand particles (gray).

postulated that for biomass particles bigger than 1 mm in diameter, the internal heat transfer and secondary pyrolysis reactions are important.

2. Secondary tar reactions in the gas phase are not taken into account. A first simple criterion for the significance of secondary tar reactions in the gas phase of the reactor is given by Lathouwers and Bellan.[28] They proposed that the tar-to-gas conversion mechanism is of importance as long as

$$\tau_R/\tau_t = \frac{Z}{u_0} A_t \exp(-E_t/R_u T_f) > 0.1, \quad (12)$$

where τ_R is the mean gas residence time, τ_t is the tar conversion time scale, $A_t = 4.28e^{+6}$ 1/s and $E_t = 108.0$ kJ/mol[30]. In this work, for a temperature of 758 K and a fluidization velocity of 0.76 m/s, $\tau_R/\tau_t \approx 0.09$. They further pointed out that small lab-scale reactors are able to operate without significant tar-to-gas conversion while secondary tar reactions in large-scale reactors are significant due to higher domain heights Z.

3. Shrinkage due to drying (4–7%), for particles used in this work, is too small to significantly impact drying times and, therefore, has a negligible impact on the final product yield.[35]

Results and Discussion

Work has been carried out to investigate the effects of different distributor plates and their impact on the bed hydrodynamics. Then, the thermochemical conversion from solid virgin wood particles to condensible vapors (bio-oil) has been studied under different conditions. This includes different (1) superficial fluidization velocities and therefore bubbling bed behaviors, (2) biomass moisture contents, and (3) reactor temperatures. Analysis has been conducted based on the origin of entrained particles and the underlying mechanism for entrainment in this small-scale reactor.

Fluidization of sand

Figure 5 depicts the fluidization of the sand bed for different superficial velocities and inlet distributor plates. The higher inlet velocity ($u_0 = 0.76$ m/s) has been chosen according to experiments and provokes a rather vigorous fluidization. The bubble size is usually big ($d_B > D/3$) and the fine sand particles are raining down mainly at the cylinder walls indicating an axial slugging behavior.[49] A rather faint bubble formation is observed for a superficial velocity of $u_0 = 0.365$ m/s predominantly in the lower part of the reactor. Herein, bubbles still contain a rather high fraction of solids.

The section in which the biomass is fed into the fluidized bed, as illustrated in Figure 4, is included in any study throughout this work. Because of different packing and space holding for future biomass feeding, a bypass is created at the left side of the bed (see Figure 5). This triggers a higher frequency of bubble formation to the left and affects the overall bubbling bed behavior. This behavior is believed to have a negligible effect on averaged degradation statistics and is not unlikely to be present in experiments as well.

Further simulations have been conducted to analyse the hydrodynamic behavior of two different mass flow rates (26 L/min and 52 L/min equivalent to $u_0 = 0.365$ m/s and $u_0 = 0.76$ m/s) on two different inlets where the flow passes only selected orifices/cells (see Figure 3) or the entire surface (uniform plug flow). Under constant mass flow rate, no significant difference related to the bed and bubble characteristics has been observed. However, a clear distinction between channelling and plug flow is observed in the bottom part of the bed. Channelling flow above orifices bridges dead zones (hardly moving particles at the bottom) and generates bubbles preferably in the middle of the bed causing slightly larger disturbance and better mixing. Flat plug flow bubbles almost stretching across the reactor are created right at the distributor plate itself and grow to rather spherically shaped bubbles when they burst the bed surface. In this 100 g/h rig, bubble characteristics are fairly similar in the upper bed section regardless of the distributor plate used. It has been found that the perforated distributor plate slightly improves mixing in the bottom regions of the bed but negligible differences have been found in terms of the overall particle heat transfer and therefore bio-oil yield. Biomass does not even reach the bottom of faintly bubbling beds and if good mixing is achieved as in vigorous bubbling beds, biomass particles are similarly in contact with sand using plug flow inlets.

Injection, segregation, and drying prior pyrolysis

Biomass is continuously pushed by a screw feeder into the reactor without carrier gas and the initial particle temperature is assumed to be 323 K. Figure 6 shows how biomass particles change their location right after injection. To the left, a general segregation effect is shown where biomass ($\rho \approx 660$ kg/m^3) rises inside the dense sand bed ($\rho_s \approx 2600$ kg/m^3). In this faintly bubbling bed, biomass particles remain together as long as the "biomass bubble" is big enough to rise through the dense sand bed. The separation process between the biomass bubble and newly injected particles is also dependent on how much gas bubbles interfere with the process. There are hardly any biomass particles traveling on their own-except in the biomass bubble wake. At the top of the bed a growing layer of biomass particles are created as long as gas bubbles remain small and only

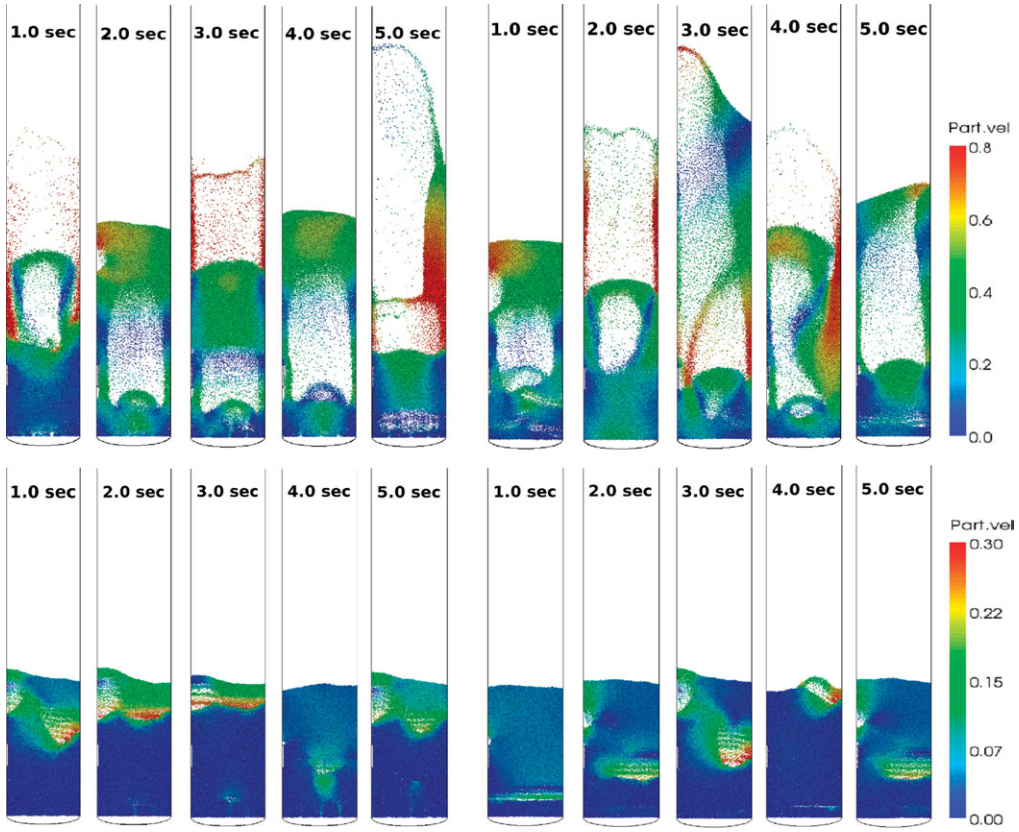

Figure 5. Particle velocity magnitude (m/s) under different fluidization conditions—u_0 = 0.76 m/s at the top and u_0 = 0.365 m/s at the bottom; perforated distributor plate (Fig. 3) to the left and plug flow inlet to the right.

[Color figure can be viewed in the online issue, which is available at wileyonlinelibrary.com.]

light mixing takes place. In that case, biomass particles are surrounded mostly by other cold biomass particles and pyrolysis is delayed and turns gradually into slow pyrolysis. To the right of Figure 6, injection into a vigorous bubbling bed with strong bubble formation is shown. The large gas bubble originated from the left bottom corner quickly expands to the right and upward direction to reach the freeboard. Such bubbles allow very efficient mixing-particles are literally torn into the gas bubble with high gas velocities and causes disturbance and therefore good particle mixing. This is particularly the case when the gas volume migrates to upper bed areas and gains momentum. The figure shows only particles which have not been completely dried ($X > 0.005$), however all other biomass particles are well distributed throughout the bed (compare Figure 9). Biomass bubbles are far smaller and likely being destroyed quickly due to good mixing and they hardly reach the top of the bed in clusters. Particle velocities can be far higher in vigorous bubbling beds.

Bubbling fluidized beds are known for their good heat transfer while circulating beds are usually very effective in mixing. The faintly bubbling bed simulation shows very high heat-transfer coefficients around 1000 W/m^2 K, however drying and pyrolysis is less effective lacking in sufficient disturbance and local exchange between sand and biomass. Figure 6 reveals the moisture content of biomass particles and it can be seen that biomass particles inside clusters (left picture) have a rather uniform high moisture content while an outer thin biomass bubble layer with direct contact to the sand phase shows only little water left. As particles are very small, their overall heat transfer surface area even locally is large and the convective heat transfer is high so that the gas temperature quickly adapts the local particle temperature. As shown in the figure, a distance of two or three particles ($\approx$ 1 mm) from the sand phase can be enough to thermally isolate biomass particles, also partially as they absorb latent heat.

Table 4 summarizes the time required to dry wet biomass particles in differently fluidized beds. These values are

Figure 6. Biomass particles inside the dense bubbling sand bed during the drying process for u_0 = 0.365 m/s (left) and u_0 = 0.76 m/s (right).

The color scale refers to the biomass moisture content X and particle velocities (as arrows) shortly after injection. The sand phase is modeled discrete but visualized non-discrete.

Table 4. Comparison of Yield Fractions (in %) Obtained in Experiments and Simulations

Bed Description	Results from Experiments			Results from Simulations						
				Pyrolysis				Drying		
	Tar	Gas	Char	H_2O	Tar	Gas	Char	Avg	Max	Min
758 K, 16.1% moisture, $u_0 = 0.76$ m/s	71.7	12.6	15.7	24.6	52.5	9.7	13.2	0.276s	0.58s	0.13s
758 K, 7.0% moisture, $u_0 = 0.76$ m/s	65.1	14.6	20.3	9.9	60.8	12.3	17.0	0.257s	0.565s	0.15s
699 K, 7.0% moisture, $u_0 = 0.76$ m/s	60.2	12.8	27.0	21.7	42.5	14.8	21.0	0.345s	0.71s	0.21s

The yield released by particles is added over all biomass particles in the simulation after 5 seconds of first biomass injection. The time required for drying has been recorded as a maximum, minimum and averaged value originating from the first batch (318 particles injected at the same time).

averaged over one batch (318 biomass particles) injected at the same time. The only difference in the first two cases is the biomass moisture content. It requires more time to evaporate more water—however, other effects like local bubble formation and segregation have an impact on the local heat transfer and drying times. It has been found that the difference related to the drying time of both cases is so close (also compare the pyrolysis part in Figure 8), that even other effects matter more than the moisture content itself. A temperature difference of the bed has a much higher effect on both drying times and pyrolysis degradation.

Fast pyrolysis modeling

Pyrolysis starts roughly 0.5–1 s after injection for the bed conditions studied (Figure 8). During that time, particles have probably left the drying region close to the inlet, characterized by the presence of many cold (new) biomass particles and the presence of lower-temperature due to latent heat absorption. Figure 7 illustrates a particle trajectory and reveals the spatial sections attributed to heating and pyrolysis. Vapor gases are released appreciably when the biomass particle temperature rises beyond 630 K. Similarly to drying, the process time for pyrolysis is strongly linked to the degree of mixing. Figure 9 compares three bubbling beds operated with different superficial velocities. The fluidization velocity is a very efficient if not the most important parameter to achieve different levels of mixing. Good mixing favors the direct contact between virgin cold biomass and hot sand and in turn allows a good heat transfer. It can be seen in Figure 9 that for higher fluidization velocities the average biomass particle temperature within 2 s of biomass feeding rises without changing other bed conditions. High tar vapor is produced by particles particularly in areas where high heat transfer is achieved—more precisely when particles are close to the sand phase and inside dense beds where the convective heat-transfer coefficient is high. Figure 14 reveals the highest tar release for dispersed particles inside the dense bed while particle clusters generally show little tar formation. The local tar formation agrees well with findings in Figure 12 where the injection area is cold and not easy to access by partially depleted biomass particles. The main local tar formation takes place in near-wall areas—except for the injection area to the left. When bubbles burst at the bed surface, they preferably rise in the middle of the bed, pushing bed particles towards the walls. In Z-direction, a vigorous bubbling bed shows always higher particle volume fractions at the bottom (averaged over time) and, therefore, tar is predominantly released in such areas. For a strongly segregated biomass phase as in the first case of Figure 9, the tar formation profile in Z-direction displays a sharp spike indicating less efficient mixing and distinct segregation.

Biomass particles reaching a maximum temperature level after slightly more than 1 s after injection as shown in Figure 10. Later in time temperature reduces due to the applied reaction heat given in Table 2. The heat-transfer coefficient is derived from the Nusselt number given in Eq. 5 and gives very high values around 1000 W/m^2 K. The heat-transfer coefficient rises slightly due to particle shrinkage as indicated by the trendline.

Table 4 compares simulation results with experimental data obtained from the Iowa State University 100 g/h pyrolyzer. The tar fraction in experiments contains water and the condensed vapor fraction while the simulation distinguishes between the water which originates from the drying process only and the condensed vapor fraction (tar) which includes water generated during the degradation process at elevated temperatures. Simulation results after 5 s of real time indicate a slightly overprediction of water and/or tar and underpredict the char yield in all three test cases when compared to experimental stady-state results. The second (758 K, $X = 7.0\%$) and third (699 K, $X = 7.0\%$) run produce the same absolute amount of water at the outlet due to the same moisture content and feeding rate applied. This indicates that the second run produces more than twice the amount of tar, gas and char together than the third one. Figure 8 indicates that this is possible although for a fully steady-state process the ratio would reduce and more char would be created. In other words, in the first 5 s biomass is not entirely converted and the remaining X_{Wood} portion contains mainly lignin which preferably turns into char; however, the relative water content would reduce. Similarly, the first run (758 K, $X = 16.1\%$) produces more than twice the amount of water compared to the second run and both undergo similar conversion during pyrolysis. Therefore, a very good agreement between experimental and simulation results has been obtained. It has to be kept in mind that simulation results are not obtained at the outlet, they are produced as the sum of all biomass particle source terms in the simulation.

It is difficult to determine the product yield directly at the outlet as char particles leave the reactor erratically and it seems that steady-state particle entrainment is reached far later than water, tar and gas yields. Because only shrinkage is considered in this simulation work it is believed that far more tiny char particles leave the reactor being created additionally by breakage and attrition. To perform simulations in a reasonable time period, a further reduction in particle size is prohibited. Figure 15 illustrates the gas composition at the outlet which matches very well with steady-state experimental data from Table 4. According to Figure 15 steady-state is reached for water. A steady-state tar and gas mass flow rate is only approximately achieved after 2.5 s as the number of biomass particles still grow and most of them only deplete slightly after 2.5 s after injection (Figure 8).

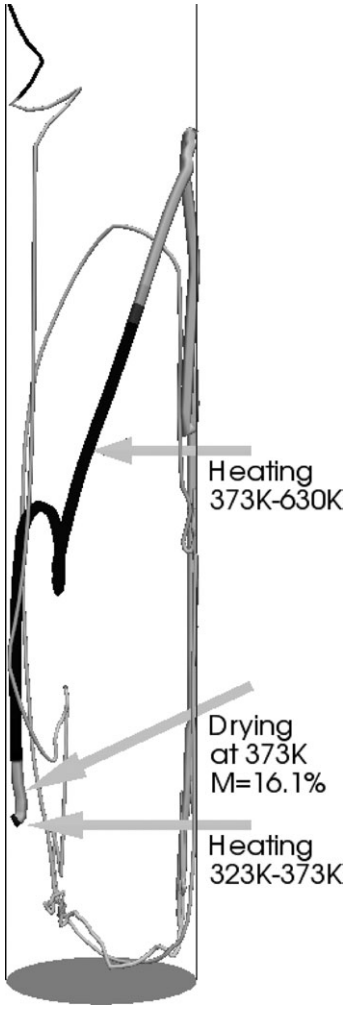

Figure 7. A single particle trajectory is illustrated showing spatial sections where heating up to 373 K (first black section), drying at 373 K (white section) and further heating to 630 K (another black section) takes place.

The particle had a moisture content of initially 16.1%. Pyrolysis prevails along the last white colored section of the trajectory and has not be seen terminated throughout any of our simulations for any particle.

Entrainment of particles

The function of the freeboard above a fluidized bed is to disengage gas and particles. Particles which fall back into the bed can only reach a maximum height above the bed transport disengagement height (TDH) as long as their terminal velocity u_t is bigger than the fluidization velocity u_0. In case of entrainment during fast pyrolysis, particles are harmful as char contains inorganics (ash) which causes fouling, corrosion, erosion, and plugging of orifices.[50] Consequently, there is an optimum reactor height—short enough to reduce the residence time of tar but tall enough to reduce particulates in bio-oil and postprocessing equipments (cyclones, filters, condensers).

Table 5 contains the superficial velocity used and the terminal velocity associated to different particles in this work. It can be seen that the terminal velocity is always higher than the superficial fluidization velocity. Although no particle entrainment has been encountered in the faintly bubbling fluidized bed model for the first 5 s of fast pyrolysis operation, entrainment becomes important in the vigorous bubbling stage as the TDH becomes greater than the actual reactor height. Due to different and unaccounted physical multiphase flow conditions in the freeboard, there is considerable quantitative disagreement between estimated TDHs, entrainment rates, etc.[23,49,51] TDH values can be calculated for the 100 g/h small-scale fluidized bed reactor with an inlet flow rate of 52/25 L/min from Baron et al.[23] (TDH = 3.94 m/1.74 m), Horio et al.[52] (both TDH = 3.33m) or Smolders and Baeyens[53] (TDH = 1.98 m/1.08 m). All of these calculated values are not dependent on particle properties and do not consider effects of a slugging regime ($d_B > D/3$) or multimodal particle composition in very small lab-scale reactors.

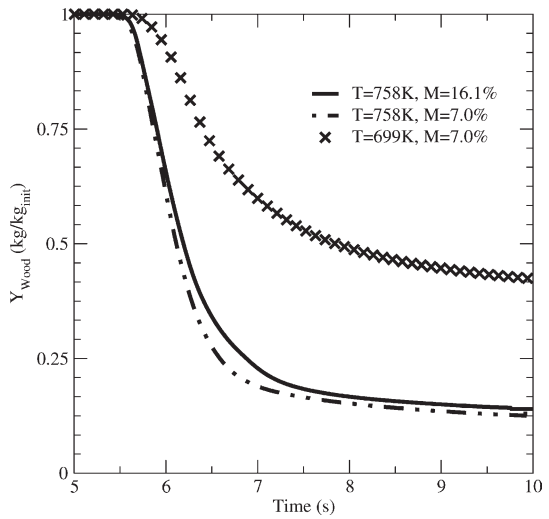

Figure 8. The remaining unreacted wood portion averaged over the first batch (318 particles) injected at 5 s.

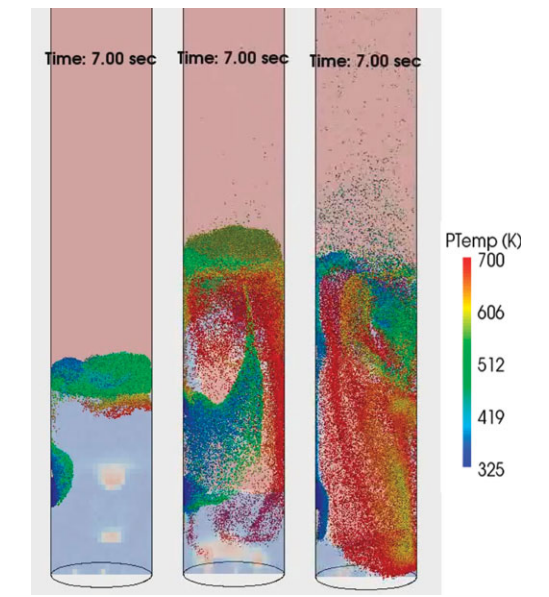

Figure 9. Biomass distribution at 7 s for different superficial fluidization velocities [u_0 = 0.356 m/s (26 L/min), u_0 = 0.61 m/s (42 L/min), u_0 = 0.76 m/s (52 L/min)].

Other conditions: T = 758 K, X = 16.1%. [Color figure can be viewed in the online issue, which is available at wileyonlinelibrary.com.]

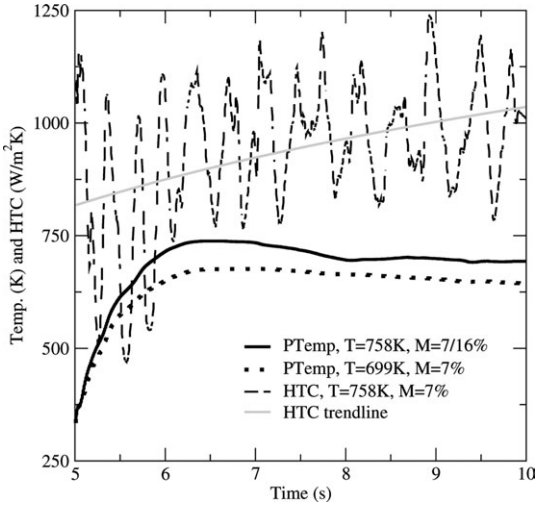

Figure 10. Particle temperature and convective heat-transfer coefficient averaged over one batch of particles (318 particles).

Other conditions: $u_0 = 0.76$ m/s.

Despite of the uncertainty of calculated TDHs, theoretical expectations and experimental results confirm the qualitative entrainment behavior modeled in this work.

The vigorous bubbling bed is characterized by its large bubble development and its intensive bubble eruptions by which light particles often reach the upper freeboard area where they are eventually entrained. Figure 16 captures three different moments before entrainment of several large particles. The left figure illustrates a huge bubble formation at the bottom—probably one of the key prerequisites to obtain high velocities necessary for entrainment. Four particles are highlighted which are going to be entrained. All originate from different locations. Later in time, the upper three particles come very close together on the bubble dome and will be entrained similarly. In slugging beds, it is expected that mainly roof solids are thrown into the freeboard while wake particles are not.[49] The fourth lower particle gains height by

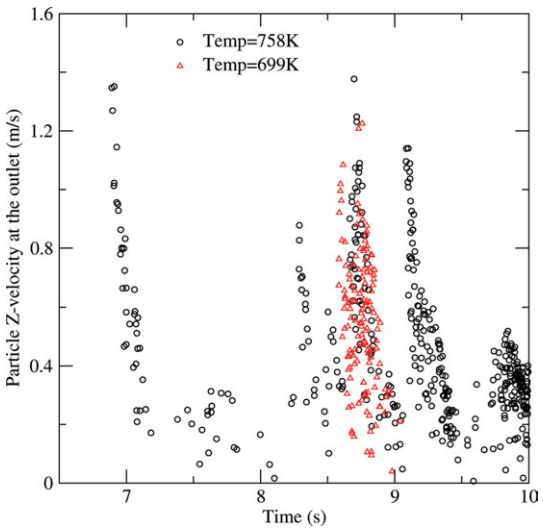

Figure 11. Z-velocity of entrained particles at the outlet of the reactor.

Other conditions: $u_0 = 0.76$ m/s, $X = 7.0\%$. [Color figure can be viewed in the online issue, which is available at wileyonlinelibrary.com.]

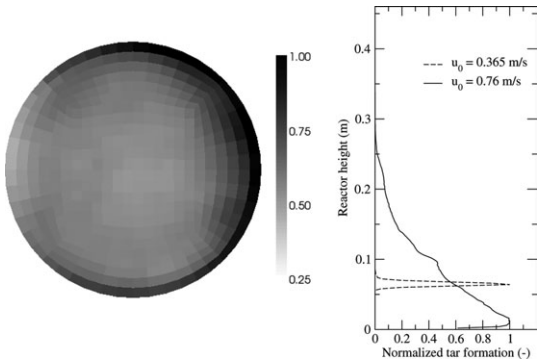

Figure 12. Left: spatial tar formation in X-Y plane, where each cell value represents the sum of all cells in Z-direction divided by the maximum value found in the X-Y plane (normalized) for $u_0 = 0.76$ m/s and right: normalized spatial tar formation in Z-direction.

ending up in the middle of the bubble where it has been accelerated by the fast upward moving gas flow. These gas velocities can easily approach 4 m/s while operating the bed with a superficial velocity of 0.76 m/s only.

Before entrainment occurs, most particles change their direction due to collisions just above or near the top of the bed. They can experience even negative Z-velocities as long as they are repositioned (by collisions) into a fast upward moving gas stream (originating from a big bubble). Numerous potential collision partners are available in the lower freeboard region while the particle concentration reduces exponentially with the freeboard height. Hundreds of entrained particles have been looked at throughout this work having in common that they are positioned rather in the middle of the X-Y plane and do not collide on its recent path before leaving the reactor. The upper freeboard usually displays a very flat and characteristic rather laminar Hagen-Poiseuille flow profile in which particles experience very low relative velocities regardless of their current location. In

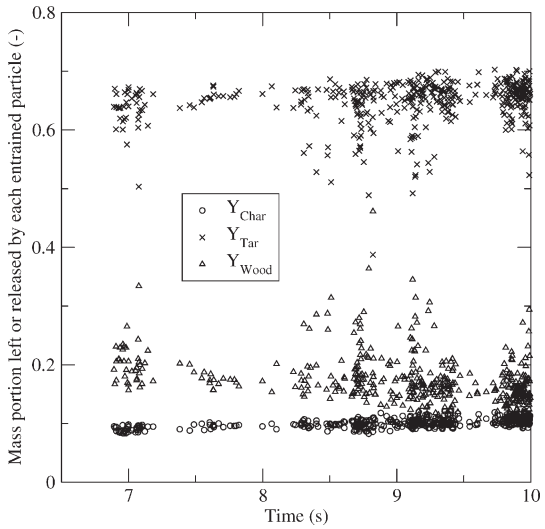

Figure 13. Remaining wood and char fraction of entrained particles and the released tar yield fraction based on the initial wood mass.

The fraction of released noncondensible gases is not shown. Other conditions: $u_0 = 0.76$ m/s, $X = 7.0\%$, T = 758 K.

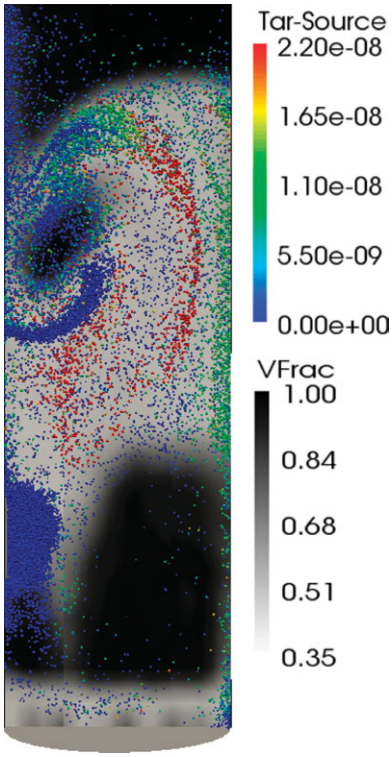

Figure 14. Tar source terms (kg/s) of individual biomass particles inside the bed.

Unlike common practice, herein black background color refers to high gas volume fractions while gray color refers to low gas volume fractions. Bed conditions: u_0 = 0.76 m/s, X = 7.0%, T = 758 K. [Color figure can be viewed in the online issue, which is available at wileyonlinelibrary.com.]

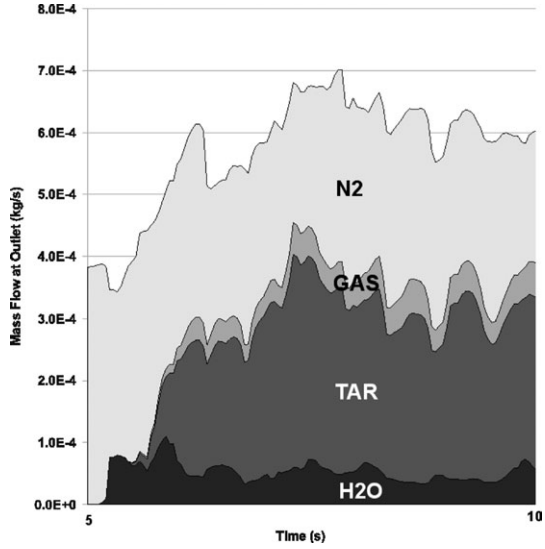

Figure 15. Gas composition at the reactor outlet obtained from the simulation.

Lighter noncondensible gases such as CO_2, CO, H_2, and CH_4 are summarized as GAS. Tar might also include a smaller water fraction. Other conditions: u_0 = 0.76 m/s, X = 7.0%, T = 758 K.

case of collisions, particles are more likely to change their directions and finally fall back (preferably near the wall) into the bed. Figure 16 shows 30 trajectories of particles which are entrained in the same time-window between 8.60 and 8.70 s of reactor operation.

After 5 s of first biomass injection into the second fluidized bed (T = 758 K, X = 7.0%, and u_0 = 0.76 m/s) the following information can be obtained from the simulation. A total number of 188,781 biomass particles remain in the reactor while only 429 particles have left the reactor through the outlet. Based on the first batch of 318 biomass particles, only eight particles have left the reactor. Figure 11 illustrates the Z-velocity of entrained particles. It can be seen that particles are getting entrained periodically in clusters depending on the eruption of very large bubbles. Although the hydrodynamic behavior is similar between the second and third (T = 699 K, X = 7.0%, and u_0 = 0.76 m/s) simulation run, entrainment results are different. In the third run, the conversion of particles to lower densities takes much longer (Figure 8) and entrainment of higher density biomass has hardly been observed throughout any simulation. All particles entrained in the third simulation case have a higher average density and have been entrained almost at the same time originating from one large bubble. For the second simulation case, the composition of entrained particles are summarized in Figure 13. The remaining wood fraction can be associated with mainly lignin which slowly reacts in time representing roughly 20% of the original particle mass. This fraction slightly reduces in time which indicates that steady-state has not been reached completely. The char and tar mass fraction grow slightly accordingly. These results indicate that the majority of entrained particles are expected to have a similar yield fraction.

Conclusion

A DEM/CFD model has been presented which is able to model the thermochemical degradation of biomass inside a lab-scale bubbling fluidized bed reactor containing roughly 0.8 million particles. The model treats all particles as spherical discrete elements where each is associated with a range of physical and material properties. This allows detailed investigations at different scale levels with high precision. Collisions, chemical reactions, fluid- and thermodynamic interactions are solved during biomass depletion and shrinkage. Such sophistication allows to study fast pyrolysis from a novel perspective, and to raise the level of understanding. The model has been validated with experimental data.

First, bed hydrodynamics have been modeled depending on different inlet distributor plates at the bottom of the bed. Only small changes in the motion of bed particles have been recognized without changing the particle volume fraction much and it is strongly believed that this has hardly any effect (in the reactor studied) on the final pyrolysis yield composition.

Table 5. Terminal Velocity of Sand, Virgin Wood, and Char Particles

Criteria	Formula	Sand (m/s)	Dry Virgin Wood (m/s)	Char Residue (m/s)
Terminal velocity (u_0 = 0.365 m/s)	$u_t = \sqrt{\frac{4}{3}\frac{d_p g(\rho_p - \rho_f)}{\rho_f C_D}}$	2.45	1.19	0.574
Terminal velocity (u_0 = 0.76 m/s)		3.20	1.56	0.766

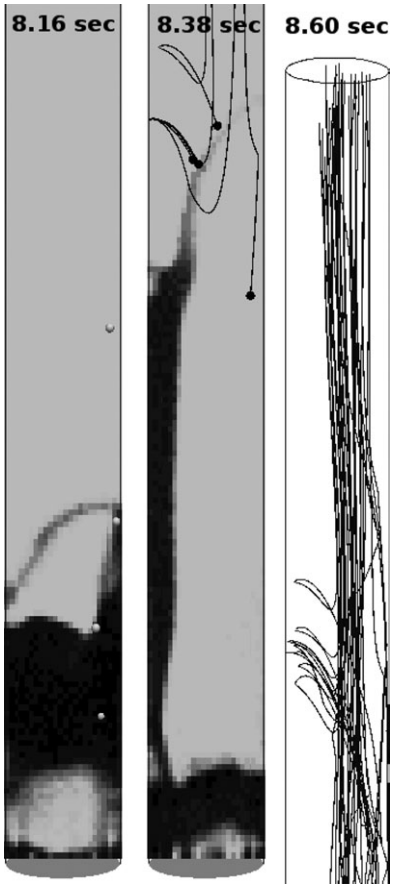

Figure 16. Four selected biomass particles and their way through the reactor inside the dense bubbling sand bed which are going to be entrained later in time (at ≈ 8.60 s).

The right figure shows numerous particle trajectories which are entrained approximately at the same time.

Therefore, modeling pyrolysis under plug-flow conditions in slugging beds should not result in erroneous predictions.

It has been found that the fluidization velocity is a very important parameter which affects mixing and in turn heat transfer to particles. The fluidization velocity should not be chosen close to the minimum fluidization velocity to avoid segregation and small bio-oil yield fractions. Two cases with different bed temperatures have been compared where secondary tar reactions are not important. In agreement with the literature,[28,42] it has been shown that the bed temperature strongly affects the yield composition-obtaining generally a good yield around 750 K. Simulations undertaken in the scope of this work indicate that the biomass moisture content has hardly any effect on the pyrolysis process itself but does affect the water content in the final oil fraction. The product yields obtained in experiments and simulations are in good agreement for all conditions tested. Taking into account an expected slight increase in char and a slightly smaller water content for a steady-state result, both experiments and simulations would be in even better agreement.

Although particle entrainment results are far from being steady-state, the main characteristics of the entrainment process have been studied. Generally it is assumed, that particles in the bed are splashed into the freeboard when bubbles burst at the surface.[19] However, in this lab-scale fluidized bed model, it has been observed that the size of the bubble determines the fast upward moving gas stream responsible for carrying the particles up to the top of the bed. Rather free moving particles positioned at the bubble dome or inside the bubble itself are more likely to be entrained. No entrained particles originate from the bubble wake. Entrained particles leave the reactor periodically in small clusters.

The 3-D simulations undertaken are able to reliably reproduce overall conditions encountered in experiments and deliver a powerful tool to understand and examine local and global effects and aspects relevant to further optimize these complex processes.

Acknowledgments

The authors gratefully acknowledge the financial support from EPSRC (Grant No. EP/G034281/1), EU FP7 ECOFUEL project (246772) and the Leverhulme-Royal Society Africa Award. Supercomputing resources on HECToR are highly appreciated from the EPSRC grant No. EP/I000801/1.

Notation

Roman symbols

A = surface area of a particle (m^2)
C_D = drag coefficient (−)
c_p = specific heat capacity (J/kg K)
d = diameter (m)
k = reaction rate (1/s)
g = gravitational acceleration (m/s^2)
H = reaction heat or latent heat (J/kg)
h = heat transfer coefficient (W/m^2 K)
m = particle mass (kg)
P = local normal pressure (N/m^2)
Pr = Prandtl number $Pr = c_p\mu_f/\lambda_f$ (−)
Q = energy source term (W)
R_u = universal gas constant (8.314 J/mol K)
Re_p = particle Reynolds number (−)
$Re_p = |u_p - \tilde{u_f}|d_p\rho_f/\mu_f$ (−)
S = species source term (kg/s)
T = temperature (K)
t = time (s)
u = velocity (m/s)
v = char formation mass ratio for reaction k_3 (−)
X = mass fraction (kg/kg_{DS})
Y = mass fraction (kg/kg_{tot})

Greek letters

β = interphase momentum transfer coefficient (kg/m^3 s)
ε = fluid volume fraction (−)
Γ = diffusion coefficient ($\Gamma_f = \frac{\nu_f}{0.7\rho_f}$) ($m^2/s$)
λ = thermal heat conductivity (W/mK)
μ = dynamic viscosity (kg/ms)
ρ = density (kg/m^3)
$\bar{\bar{\tau}}$ = shear stress tensor (N/m^2)
ω = emissivity (−)

Subscripts

A = active component (AC = active cellulose, etc.)
C = cellulose
evap = evaporation
f = fluid
H = hemicellulose
L = Lignin
p = particle
DS = dry solid (virgin wood) material
t = tar
tot = total

Abbreviations

CFD = computational fluid dynamics
DEM = discrete element method
PSD = particle size distribution
TDH = transport disengaging height

Literature Cited

1. Laird DA, Brown RC, Amonette JA, Lehmann J. Review of the pyrolysis platform for co-producing bio-oil and bio-char. *Biofuels Bioproducts Biorefining*. 2009;3:547–562.
2. van der Hoef MA, van Sint Annaland M, Deen NG, Kuipers JAM. Numerical simulation of dense gas-solid fluidised beds: a multiscale modelling strategy. *Annu Rev Fluid Mech*. 2008;40:47–70.
3. Passalacqua A, Fox RO, Garg R, Subramaniam S. A fully coupled quadrature-based moment method for dilute to moderate dilute fluid-particle flows. *Chem Eng Sci*. 2010;65:2267–2283.
4. Desjardin O, Fox RO, Villedieu P. A quadrature-based momentum method for dilute fluid-particle flows. *J Comput Phys*. 2008;227:2524–2539.
5. Cundall PA, Strack ODL. A discrete numerical model for granular assemblies. *Geotechnique*. 1979;29:47–65.
6. Deen NG, van Sint Annaland M, Van der Hoef MA, Kuipers JAM. Review of discrete particle modeling of fluidized beds. *Chem Eng Sci*. 2007;62:28–44.
7. van Wachem BGM, Schouten JC, Krishna R, van den Bleek CM. Experimental validation of Lagrangian-Eulerian simulations of fluidized beds. *Powder Technol*. 2001;116:155–165.
8. Feng YQ, Yu AB. Effect of bed thickness on the segregation behavior of particle mixtures in a gas fluidized bed. *Ind Eng Chem Res*. 2010;49:3459–3468.
9. Freige FY, Langston PA. Integration schemes and damping algorithms in distinct element models. *Adv Powder Technol*. 2004;15:227–245.
10. Zhou ZY, Yu AB, Zulli P. Particle scale study of heat transfer in packed and bubbling fluidised beds. *AIChE J*. 2009;55:868–884.
11. Zhou H, Flamant G, Gauthier D. DEM-LES simulation of coal combustion in a bubbling fluidized bed Part II: coal combustion at the particle level. *Chem Eng Sci*. 2004;59:4205–4215.
12. Rong D, Horio M. DEM simulation of char combustion in a fluidized bed. Presented at the 2nd International Conference on CFD in the Minerals and Process Industries, Dec. 6–8, 1999, Melbourne, Australia.
13. Oevermann M, Gerber S, Behrendt F. Euler-Lagrange/DEM simulation of wood gasification in a bubbling fluidized bed reactor. *Particuology*. 2009;7:307–316.
14. Rabinovich OS, Borodulya VA, Vinogradov LM, Korban VV. Fast pyrolysis of an ensemble of biomass particles in a fluidized bed. *J Eng Phys Thermophys*. 2010;83:694–704.
15. Papadikis K, Gu S, Bridgwater AV. CFD modelling of fast pyrolysis of biomass in fluidised bed reactors. Part A Eulerian computation of momentum transport in bubbling fluidised beds. *Chem Eng Sci*. 2008;63:4218–4227.
16. Papadikis K, Gu S, Bridgwater AV. CFD modelling of fast pyrolysis of biomass in fluidised bed reactors. Part B Heat, momentum and mass transport in bubbling fluidised beds. *Chem Eng Sci*. 2009;64:1036–1045.
17. Papadikis K, Gu S, Bridgwater AV. CFD modelling of fast pyrolysis of biomass in fluidised bed reactors: modelling the impact of biomass shrinkage. *Chem Eng J*. 2009;149:417–427.
18. Di Blasi C. Modeling chemical and physical processes of wood and biomass pyrolysis. *Prog Energy Combust Sci*. 2008;34:47–90.
19. Wen CY, Chen LH. Fluidized bed freeboard phenomena: entrainment and elutriation. *AIChE J*. 1982;28:117–128.
20. Wen CY, Yu YH. Mechanics of fluidization. *Chem Eng Progr Symp Ser*. 1966;62:100–111.
21. van der Hoef MA, Ye M, van Sint Annaland M, Andrews IV AT, Sundaresan S, Kuipers JAM. Multi-scale modeling of gas-fluidized beds. *Adv Chem Eng*. 2006;31:65–149.
22. van Wachem BGM, Schouten JC, van den Bleek CM, Krishna R, Sinclair JL. Comparative analysis of CFD models of dense gas-solid systems. *AIChE J*. 2001;47:1035–1051.
23. Baron T, Briens CL, Bergougnou MA. Study on the transport disengagement height. *Can J Chem Eng*. 1988;66:749–760.
24. Tsuji Y, Tanaka T, Ishida T. Lagrangian numerical simulation of plug flow of cohesionless particles in a horizontal pipe. *Powder Technol*. 1992;71:239–250.
25. Mindlin RD, Deresiewicz H. Elastic spheres in contact under varying oblique forces. *J Appl Mech Trans ASME*. 1953;20:327–344.
26. Bruchmüller J, Gu S, Luo KH, van Wachem BGM. Discrete element method for multiscale modelling. *J Multiscale Model*. 2010;2:147–162.
27. Mikami T, Kamiya H, Horio M. Numerical simulation of cohesive powder behavior in a fluidized bed. *Chem Eng Sci*. 1998;53:1927–1940.
28. Lathouwers D, Bellan J. Yield optimization and scaling of fluidized beds for tar production from biomass. *Energy Fuels*. 2001;15:1247–1262.
29. Gunn DJ. Transfer of heat or mass to particles in fixed and fluidized beds. *Int J Heat Mass Transfer*. 1978;21:467–476.
30. Miller RS, Bellan J. A generalized biomass pyrolysis model based on superimposed cellulose, hemicellulose and lignin kinetics. *Combust Sci Technol*. 1997;126:97–137.
31. Bradbury AGW, Sakai Y, Shafizadeh F. Kinetic model for pyrolysis of cellulose. *J Appl Polym Sci*. 1979;23:3271–80.
32. Koufopanos CA, Papayannakos N, Maschio G, Lucchesi A. Modelling of the pyrolysis of biomass particles. Studies on kinetics, thermal and heat transfer effects. *Can J Chem Eng*. 1991;69:907–915.
33. Rabinovich OS, Korban VV, Pal'chenok GI, Khorol'skaya OP. Modeling of fast pyrolysis of a single biomass particle in an inert boiling bed. *J Eng Phys Thermophys*. 2009;82:621–631.
34. Bellais M, Davidsson KO, Liliedahl T, Sjöström K, Pettersson JBC. Pyrolysis of large wood particles: a study of shrinkage importance in simulations. *Fuel*. 2003;82:1541–1548.
35. Bryden KM, Hagge MJ. Modeling the combined impact of moisture and char shrinkage on the pyrolysis of a biomass particle. *Fuel*. 2003;82:1633–1644.
36. Di Blasi C. Heat, momentum and mass transport through a shrinking biomass particle exposed to thermal radiation. *Chem Eng Sci*. 1995;51:1121–1132.
37. Christensen D, Vervloet D, Nijenhuis J, van Wachem BGM, van Ommen JR, Coppens MO. Insights in distributed secondary gas injection in a bubbling fluidized bed via discrete particle simulations. *Powder Technol*. 2008;183:454–466.
38. Bruchmüller J, van Wachem BGM, Gu S, Luo KH. Modelling discrete fragmentation of brittle particles. *Powder Technol*. 2011;208:731–739.
39. Allen MP, Tildesley DJ. *Computer simulation of liquids*. Oxford, U.K.: Oxford University Press, 1990.
40. Tsuji Y, Kawaguchi T, Tanaka T. Discrete particle simulation of two-dimensional fluidized beds. *Powder Technol*. 1993;77:79–87.
41. Rhie CM, Chow WI. Numerical study of the turbulent flow past an airfoil with trailing edge separation. *AIAA J*. 1983;21:1525–1532.
42. Xue Q, Heindel TJ, Fox RO. A CFD model for biomass fast pyrolysis in fluidized-bed reactors. *Chem Eng Sci*. 2011;66:2440–2452.
43. Gardner DG, Generella NC, Gunnells DW, Welcott MP. Dynamic wettability of wood. *Langmuir, Am Chem Soc*. 1991;7:2498–2502.
44. Wenzl H. *The chemical technology of wood*. New York: Academic Press, 1970.
45. Perry RH, Green D. *Perry's Chemical Engineers' Handbook*, 6th ed. New York: McGraw-Hill, 1984.
46. Flamant G, Lu J, Variot B. Towards a generalized model for vertical walls to gas-solid fluidized beds heat transfer-II. Radiative transfer and temperature effects. *Chem Eng Sci*. 1993;48:2493–2503.
47. Pyle DL, Zaror CA. Heat transfer and kinetics in the low temperature pyrolysis of solids. *Chem Eng Sci*. 1984;39:147–158.
48. Zhou H, Flamant G, Gauthier D. DEM-LES of coal combustion in a bubbling fluidized bed Part I: gas-particle turbulent flow structure. *Chem Eng Sci*. 2004;59:4205–4215.
49. Kunii D, Levenspiel O. *Fluidization Engineering*, 2nd ed. Boston: Butterworth-Heinemann, 2005.
50. Hoekstra E, Hogendoorn KJA, Wang X, et al. Fast pyrolysis of biomass in a fluidized bed reactor: in situ filtering of the vapors. *Ind Eng Chem Res*. 2009;48:4744–4756.
51. Smolders K, Baeyens J. Elutriation of fines from gas fluidized beds: mechanisms of elutriation and effect of freeboard geometry. *Powder Technol*. 1997;92:35–46.
52. Horio M, Taki A, Hsieh YS and Muchi I. Elutriation and particle transport through the freeboard of a gas-solid fluidized bed. in *Fluidization*, Grace JR and Matsen JM, eds., New York: Plenum Press, 1980.
53. Smolders K, Baeyens J. Continuous monitoring of particle emissions by means of a tribo-electric probe. *Powder Handling Process*. 1997;9:123–127.

Manuscript received Jun. 28, 2011, revision received Sept. 28, 2011, and final revision received Nov. 15, 2011.